High Power Laser Science and Engineering, (2026), Vol. 14, e13, 10 pages.
doi:10.1017/hpl.2025.10099

RESEARCH ARTICLE

New scheme for inertial confinement fusion laser drivers based on a spatiotemporal partially coherent multi-mode source and its prospects

Jianqiang Zhu, Yanli Zhang, Xiuqing Jiang, Zhixiang Zhang, Lin Yang, Dajie Huang, Tao Feng, Hui Wei, Chong Liu, Guowen Zhang, Qi Zhang, Zijian Cui, Xiuping Zhang, Shouying Xu, Hua Tao, Bingyan Wang, Dianyuan Fan, and Xiaoqi Zhang

Key Laboratory on High Power Laser and Physics, Shanghai Institute of Optics and Fine Mechanics, Chinese Academy of Sciences, Shanghai, China

(Received 5 September 2025; revised 15 October 2025; accepted 28 November 2025)

Abstract

The traditional design of laser drivers for inertial confinement fusion (ICF) is highly dependent on coherent laser light fields, which have significant advantages in achieving harmonic conversion and enhancing amplification efficiency. However, they also bring the core challenge of achieving uniform irradiation. This paper investigates the dynamic evolution process of uniform irradiation of multi-mode spatiotemporal light fields and analyzes the influence mechanism of spatiotemporal coherence on irradiation uniformity with different integration times. By balancing the relationship between the spatiotemporal coherence of the light field and uniform irradiation, we explore a possible scheme to alleviate the beam smoothing problem while satisfying the basic requirements of laser amplification and high-efficiency harmonic conversion. Based on this scheme, the overall architecture of the ICF laser driver is constructed.

Keywords: beam smoothing; inertial confinement fusion laser driver; multi-mode spatiotemporal light fields; spatiotemporal partially coherent light

1. Introduction

Owing to the high coherence and brightness of lasers, the concept of laser-driven inertial fusion has been proposed since the advent of lasers in the 1960s[1,2]. In 2022, 80 years later, the National Ignition Facility (NIF) at Lawrence Livermore National Laboratory achieved a target gain of $G > 1$, and in April 2025, it set a new fusion yield record of 8.6 MJ[3,4], demonstrating the feasibility of laser-driven inertial fusion. A key challenge for successful laser-driven inertial fusion is achieving high-symmetry implosion and high-energy output for both indirect and direct drives. High-symmetry implosion requires the avoidance of defects in target fabrication and necessitates uniform laser irradiation to suppress the detrimental effects of laser–plasma instabilities, such as Rayleigh–Taylor instability, cross-beam energy transfer (CBET), stimulated Raman scattering (SRS) and two-plasmon decay (TPD). This requirement is particularly critical for future higher-energy direct drives and indirect drives[5,6].

Currently, mainstream inertial confinement fusion (ICF) laser drivers predominantly employ techniques to achieve uniform irradiation[7–12] such as continuous phase plates (CPPs), lens arrays (LAs), polarization smoothing (PS), smoothing by spectral dispersion (SSD), and an induced spatial incoherence (ISI) scheme. CPPs and LAs located in the final optical system are classified as spatial smoothing methods. These methods can increase the focal spot size of coherent light according to specific contour shapes; however, the focal spot itself remains a highly modulated speckle pattern. SSD and ISI are referred to as temporal smoothing methods. The basic processing approach of this

Correspondence to: Y. L. Zhang, X. P. Zhang and X. Q. Zhang, Key Laboratory on High Power Laser and Physics, Shanghai Institute of Optics and Fine Mechanics, Chinese Academy of Sciences, Shanghai 201800, China. Emails: zhangyl@siom.ac.cn (Y. L. Zhang); 13817756475@163.com (X. P. Zhang); zhangxq_2025@163.com (X. Q. Zhang)

© The Author(s), 2026. Published by Cambridge University Press in association with Chinese Laser Press. This is an Open Access article, distributed under the terms of the Creative Commons Attribution licence (https://creativecommons.org/licenses/by/4.0), which permits unrestricted re-use, distribution and reproduction, provided the original article is properly cited.

https://doi.org/10.1017/hpl.2025.10099 Published online by Cambridge University Press

method involves increasing the laser bandwidth; typically, the spatial smoothing method is combined to obtain the desired spot shape. Studies have demonstrated that merely increasing the laser bandwidth is insufficient to effectively eliminate fixed speckle patterns. Dynamic speckle patterns should be generated and combined with the time integration method to weaken the intensity modulation of the speckles, thereby achieving uniform irradiation of the light field.

Owing to the narrow spectral bandwidth of SSD, the root mean square (RMS) value of uniform irradiation remains at approximately 10%, which is suboptimal for direct-drive applications[7,13–16]. To address the narrow bandwidth constraints of SSD methods, in 1992, the use of an amplified spontaneous emission (ASE) oscillator, characterized by both low spatial and temporal coherence, combined with angular dispersion smoothing (ADS), resulted in the RMS of the intensity distribution in the focused beam pattern of 3.3% at the GEKKO XII facility[17,18]. In 1993, partially coherent light generated by multi-mode fibers was introduced into the GEKKO XII laser seeds. The RMS of the uniform irradiation at the NIKE facility is approximately 1% under operating conditions characterized by a bandwidth of 1–3 THz and a low spatial coherence. However, both drive devices are confronted with the problem of low-frequency conversion efficiency[19]. In 2014, the StartDriver laser driver was constructed with 10^4–10^5 individual laser beams, each exhibiting relatively narrowband performance and three to five times the diffraction limit (TDL). The RMS of beam smoothing can achieve a level of 1% while simultaneously maintaining a high efficiency in harmonic conversion with excessive multiple beams. However, the superposition of these beams introduces significant technical challenges, particularly concerning the complexity of the control systems[5].

The key to achieving beam smoothing is obtaining as many irrelevant speckle patterns as possible within a certain period. The RMS is inversely proportional to the number of uncorrelated speckle patterns N_e, that is, RMS $\propto 1/\sqrt{N_e}$. The greater the number of irrelevant speckle patterns N_e, the smaller the smoothing factor RMS. In a single-beam smoothing scheme, the pulse must have both a certain bandwidth $\Delta\lambda$ and spatial divergence angle θ, and they must be mutually coupled. This means that we should simultaneously break spatial and temporal coherence. Because N_b beams with different frequencies are superimposed, the number of irrelevant speckle patterns further increases by a factor of N_b. In recent years, spatiotemporal partially coherent light (STPCL-Mm), which is composed of multiple transverse and longitudinal modes, has attracted the interest of several scientists. This can be generated using a 4F imaging cavity laser. This STPCL-Mm has a large $\Delta\nu$ and θ. In addition, it may serve as the front-end seed of the laser-driver system to obtain relatively smooth beams in a single-beam smoothing scheme. Compared with ASE sources, STPCL-Mm can be controlled freely, and the complexity of the system can be significantly simplified[20–24]. On the basis of the above description, this study investigated the influence of the spatial and temporal coherence of STPCL-Mm on the beam smoothness under different usage conditions. In addition, it examined the relationship between the bandwidth and divergence angle of the STPCL-Mm and the third-harmonic conversion performance. Finally, a potential architecture for the STPCL-Mm laser-driving system link is proposed, providing a possible reference for simultaneously addressing the core challenges of uniform irradiation and efficient harmonic conversion.

2. Uniform illumination of STPCL-Mm

2.1. STPCL-Mm numerical model

STPCL-Mm has multiple transverse and longitudinal mode laser light fields featuring spatiotemporal coupling and three-dimensional (3D) spatiotemporal particle characteristics. We started with the spatial field correlations (mutual intensity)[25,26]: $J(x_1, x_2; t) = \langle E(x_1; t) E^*(x_2; t)\rangle \Delta\tau$, where x_1 and x_2 are two-dimensional (2D) transverse coordinates, $E(x; t)$ is the electric field at point x and time t and $\langle\cdot\rangle \Delta\tau$ denotes temporal averaging. Based on the mode superposition model, at a specific moment, the total electric field distribution of the STPCL-Mm can be expressed as the product of the spatial and temporal components[26,27]:

$$E_{\mathrm{nf}}(x, y, t) = \sum_{q=1}^{Q}\sum_{n=1}^{N}\sum_{m=1}^{M} H(\nu_0 \pm q\Delta\nu_{\mathrm{FSR}}) \times F\left[E_{mn}^{\mathrm{T}}(t)\right] e^{i2\pi(\nu_0 \pm q\nu_{\mathrm{FSR}})t} \times \sqrt{C_{mn}} u_{\mathrm{nf}-mn}(x, u)\, e^{i\varphi_{\mathrm{nf}-mn}(x,y)}. \quad (1)$$

Here, m and n are transverse-mode numbers, while q is the longitudinal mode number. The expression $H(\nu_0 \pm q\Delta\nu_{\mathrm{FSR}}) \times F\left[E_{mn}^{\mathrm{T}}(t)\right]$ corresponds to the temporal spectral distribution, and $e^{i2\pi(\nu_0 \pm q\nu_{\mathrm{FSR}})t}$ signifies the inverse Fourier transform operator to obtain the distribution of the temporal pulse. Here, $H(\nu_0 \pm q\Delta\nu_{\mathrm{FSR}})$ is the actual spectral distribution, which is regulated by the longitudinal modulus q; $F[\cdot]$ is the Fourier transform operator. $E_{mn}^{\mathrm{T}}(t) = G_{mn}(t) \times iF\left[e^{i\varphi_{mn}(\nu)}\right]$, where $G_{mn}(t)$ is a square-shaped super-Gaussian pulse: $G_{mn}(t) = e^{-\left(t^2/t_1^2\right)^8}$; $t_1 = 3$ ns denotes the pulse width and t is time; $\varphi_{mn}(\nu)$ follow a uniform probability over the interval $[0, 2\pi]$, which varies between different transverse modes indicated by m and n; C_{mn} is the spectral density ratio of the mnth order mode, as listed in Tables 1 and 2 in the Appendix; $u_{\mathrm{nf}-mn}(x, y)$ and $\varphi_{\mathrm{nf}-mn}(x, y)$ denote the spatial amplitude distribution and spatial phase of the mnth transverse mode, respectively, where $u_{\mathrm{nf}-mn}(x, y) = u_{\mathrm{nf}-m}(x) u_{\mathrm{nf}-n}(y)$,

https://doi.org/10.1017/hpl.2025.10099 Published online by Cambridge University Press

$u_{\mathrm{nf}-m}(x) = \left(\frac{2}{\pi R_{00}^2}\right)^{\frac{1}{4}} \frac{1}{(2^m m!)^{\frac{1}{2}}} \times H_m\left(\frac{x\sqrt{2}}{R_{00}}\right) \exp\left(-\frac{x^2}{R_{00}^2}\right)$; R_{00} is the radius of TEM_{00}. Equation (1) reveals a pronounced spatiotemporal coupling effect.

The laser near-field distribution of STPCL-Mm is the same as that of the coherent light flat-top super-Gaussian near-field distribution in the SG II coherent laser driver[28], adopting a laser near-field aperture of 310 mm. Under nanosecond pulse widths, all of the TEM_{mnq} modes compete without phase locking and have different initial phases. The spectral profiles of TEM_{mn} is assumed to be the same as that of $\mathrm{TEM}_{m'n'}$, differing only in the spectral density proportion C_{mn}. This mathematical construction corresponds exactly to the output mode of the 4F cavity[29–35]. Corresponding to the actual parameters of the designed self-reproducing multi-mode laser resonator, the parameter sets for C_{mn} were established, with the maximum transverse-mode orders set to $m_{\max} = n_{\max} = 33$, as shown in Tables 1 and 2 in the Appendix[36], and with the frequency interval between transverse modes (with the same q) set to 40 kHz, whereas the longitudinal mode interval was configured to 130 MHz, with the spectral profile set to eighth-order super-Gaussian.

To systematically reveal the characteristics of the multi-transverse mode and multi-longitudinal mode laser light fields, we analyzed the near-field and far-field distributions of the multi-mode and multi-wavelength beams, as shown in Figures 1 and 2. Figure 1 shows the near-field characteristics of beams with different transverse and longitudinal mode orders, demonstrating the near-field evolution of STPCL-Mm. The 3D light-field distribution of STPCL-Mm exhibited distinct spatiotemporal scattered particle characteristics. The longitudinal mode numbers govern the temporal coherence length, whereas the transverse-mode numbers determine the spatial distribution[37,38]. During consecutive time slices, substructures with different spatial particle distributions and dynamic spatial reconfigurations were observed. This competition between space and time patterns resulted in spatiotemporal decoherence characteristics, as shown in Figure 1(a). When the number of transverse modes was maintained at a certain value and the number of longitudinal modes increased, spatiotemporal particles exhibited a phenomenon of time shortening, as shown in Figure 1(b), with a decrease in temporal coherence. When the number of longitudinal modes was maintained at a certain value while the number of transverse modes was increased, the spatial particles exhibited the phenomenon of more spatial particles and the spatial coherence increased, as shown in Figure 1(c). The second-harmonic emission supports many more transverse modes than the fundamental emission, and exhibits lower spatial coherence[39]. In applications such as parallel imaging and projection display, the trade-off between the efficiency of second-harmonic emission and the spatial coherence of the light source is a key consideration. Figure 2 shows the far-field characteristics of the beams with different transverse and longitudinal mode orders. It presents the far-field evolution of STPCL-Mm. The evolution patterns of the different transverse modes were similar to those of the near-field. For multiple transverse and longitudinal modes, the spatial distribution of the far-field changed continuously over time. Within a certain time integral, the focal spot was extremely smooth, thereby achieving internal beam smoothing and reducing the complexity of the laser-driving system.

2.2. Uniform irradiation of STPCL-Mm with response to spatiotemporal coherence

To verify the compatibility of the STPCL-Mm with the traditional laser-driven architecture, we evaluated the beam smoothing effect of a CPP originally optimized for coherent lasers. For multi-transverse and multi-longitudinal mode operations, the far-field spatial distribution changed continuously over time, thereby achieving intrinsic beam smoothing and significantly reducing the complexity of the laser-driving system. Figure 3 illustrates the far-field evolution of the STPCL-Mm equipped with a CPP.

To evaluate the potential of STPCL-Mm for uniform irradiation applications, we analyzed the RMSs of the focal spot irradiated directly by STPCL-Mm, STPCL-Mm passing through a CPP and the focal spot irradiated by a coherent laser with the 2D-SSD and CPP. For comparison, the CPP designed for the coherent laser was also utilized for the STPCL-Mm. The spectra were matched in width and configured to an eighth-order hyper-Gaussian profile, with full widths at half maximum (FWHMs) of 1, 0.5 and 0.1 nm at 351 nm, respectively. The phase of the 2D-SSD can be expressed as follows:

$$\phi_{\mathrm{ssd}} = \delta_x \sin\left(2\pi \nu_{mx}\left(t + \frac{\Delta\theta_x}{\Delta\lambda}\frac{\lambda}{c}x\right)\right) + \delta_y \sin\left(2\pi \nu_{my}\left(t + \frac{\Delta\theta_y}{\Delta\lambda}\frac{\lambda}{c}y\right)\right). \quad (2)$$

Here, ν_{mx}=10.4 GHz, ν_{my}=3.3 GHz and δ_x=1.96, δ_y=6.15 are the modulation frequency and modulation depth, respectively; $\frac{\Delta\theta_x}{\Delta\lambda}\frac{\lambda}{c}$= 0.3 ps/mm, $\frac{\Delta\theta_y}{\Delta\lambda}\frac{\lambda}{c}$= 1.13 ps/mm are the variation in phase across the beam due to the angular grating dispersion. The FWHM of the spectrum of the SSD was approximately 0.1 nm. Figure 4 shows the RMSs of the uniform irradiation for different spatiotemporal coherence values over time after integration for 2 ns. Figure 4(a) shows that the RMSs of the focal spot irradiated directly by STPCL-Mm were influenced by temporal coherence and were entirely independent of spatial coherence. With a 1 nm bandwidth, the RMS decreased to below 2% after integration for 2 ns, indicating that direct irradiation by STPCL-Mm can enhance the beam smoothing effect.

https://doi.org/10.1017/hpl.2025.10099 Published online by Cambridge University Press

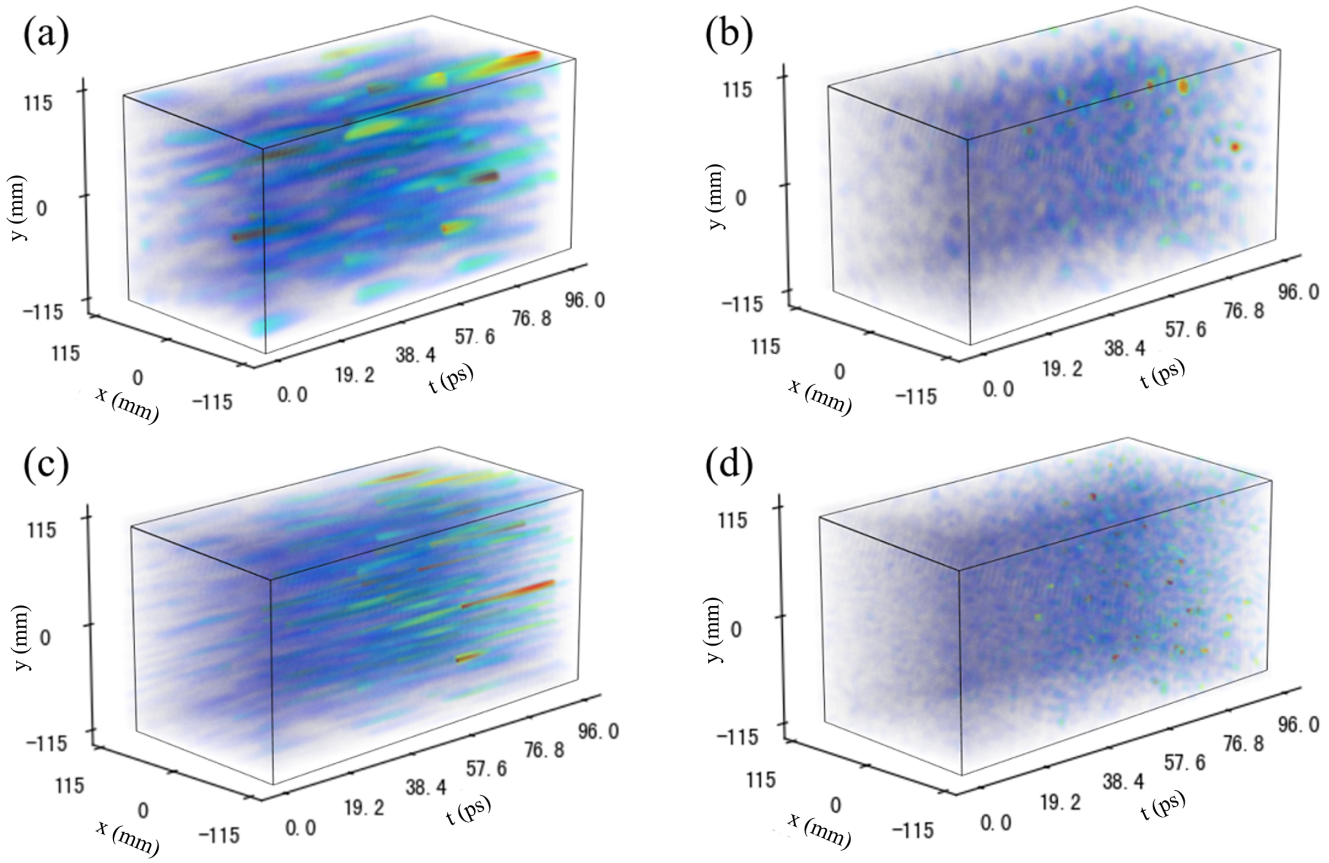


Figure 1. Near-field 3D spatiotemporal light-field distributions: (a) and (b) have a maximum transverse-mode order of 18, with longitudinal mode numbers of 468 and 3740, respectively, and spectral bandwidths of 0.25 and 2 nm, respectively; (c) and (d) have a maximum transverse-mode order of 33, with longitudinal mode numbers of 468 and 3740, respectively, and spectral bandwidths of 0.25 and 2 nm, respectively.

Furthermore, this approach simplifies the complexity of the ICF laser-driver system and offers significant advantages for practical applications. Figure 4(b) shows that the decline rates of the RMSs of uniform irradiation for STPCL-Mm passing through the CPP were influenced by both temporal coherences, whereas the minimum final RMS values were only determined by the spatial coherence in the same spectral width. With a consistent bandwidth of 0.1 nm, the decline rate of the RMSs for the 32 TDL STPCL-Mm with a CPP was faster than that of coherent lasers with a CPP and SSD, with final values (2 ns integration) of 6.6% and 7.0%, respectively. The minimum RMS of the 32 TDL STPCL-Mm with a 0.1 nm bandwidth was slightly lower than that of the 16 TDL (with $m_{\max} = n_{\max} = 18$) STPCL-Mm with a 1 nm bandwidth after integration for 1 ns. We attribute this to the higher line density in the spectrum of the 32 TDL STPCL-Mm. Each transverse mode had a distinct frequency ν_{qmn} and could alter the fine structure of the spectrum. Therefore, both the line density and bandwidth of the spectrum were important factors for determining the beam smoothness. These results show that STPCL-Mm achieves good uniform irradiation performance with a narrow bandwidth, which is particularly advantageous for high-efficiency third-harmonic generation. Thus, STPCL-Mm demonstrates significant potential as an ICF laser driver. Figure 3 shows the far-field evolution of the STPCL-Mm through the CPP. To verify the compatibility of the STPCL-Mm with the traditional laser-driving architecture, we evaluated the beam smoothing effect of a CPP originally optimized for coherent lasers. In contrast, for multi-transverse-mode and multi-longitudinal-mode operations, the spatial distribution of the far-field changed over time, achieving intrinsic beam smoothing and significantly reducing the complexity of the laser-driving system.

To reflect the impact of temporal coherence on the beam smoothing performance, we normalized the total integration time using the coherence time as a reference, as shown in Figure 4(c). The three descending curves of the RMSs for direct irradiation by STPCL-Mm, shown in Figure 4(a), were combined into a single curve. This indicated that the RMSs for direct irradiation by STPCL-Mm were solely dependent on the ratio of integration time to coherence time (RI2C) (effective irrelevant speckle pattern N_e) and were not influenced by spatial coherence. The RMSs coincided with the curve $1/\sqrt{\text{RI2C}}$. In contrast, the six declining RMS

https://doi.org/10.1017/hpl.2025.10099 Published online by Cambridge University Press

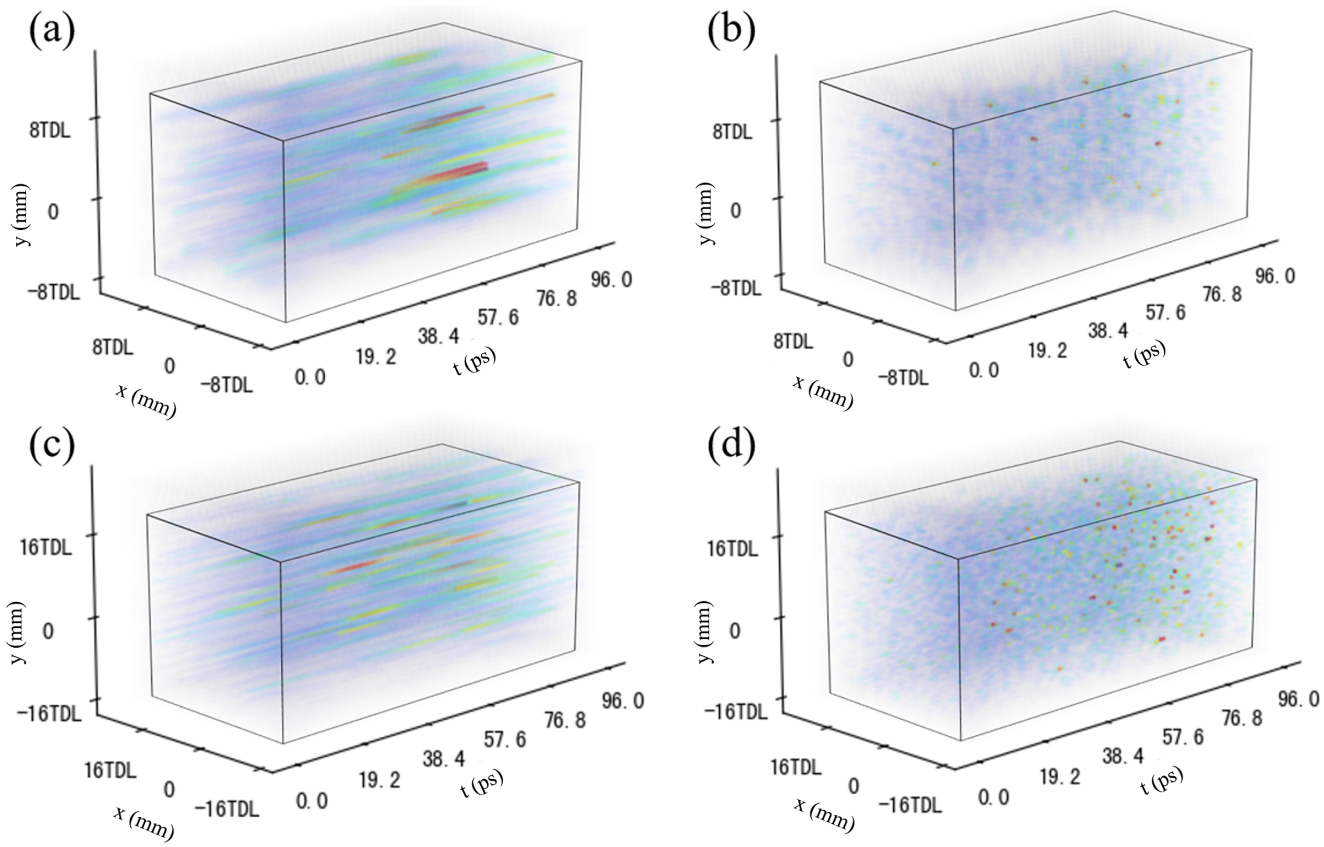


Figure 2. Far-field 3D spatiotemporal light-field distributions: (a) and (b) have a maximum transverse-mode order of 18, with longitudinal mode numbers of 468 and 3740, respectively, and spectral bandwidths of 0.25 and 2 nm, respectively; (c) and (d) have a maximum transverse-mode order of 33, with longitudinal mode numbers of 468 and 3740, respectively, and spectral bandwidths of 0.25 and 2 nm, respectively.

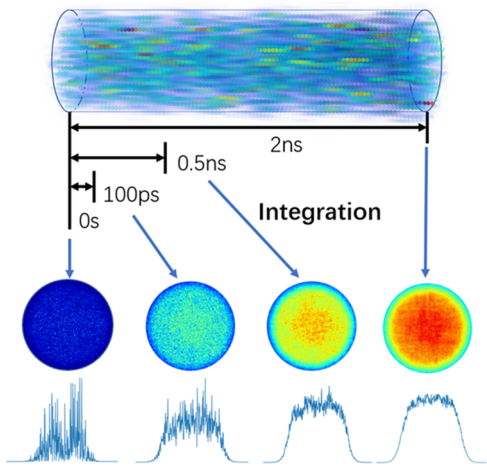


Figure 3. Three-dimensional instantaneous and time-integrated far-field distribution of STPCL-Mm equipped with a CPP. The maximum transverse-mode order was 33, the longitudinal mode number was 374 and the spectral bandwidth was 0.02 nm.

curves of the STPCL-Mm with CPP shown in Figure 4(b) converged into two curves, which depended only on spatial coherence. This suggests that a decrease in spatial coherence is advantageous only when it is affected by a CPP. The rate of decline in the RMSs of the focal spot irradiated by a coherent laser with 2D-SSD and CPP differed from that of STPCL-Mm with the CPP. We attributed this discrepancy to the different spectral shapes of 2D-SSD and STPCL-Mm despite sharing the same bandwidth[38,40,41]. Consequently, the declining trend of the RMSs was influenced by the spectral shape and fine structure, and the value of the RMSs depended on RI2C, which was determined by the coherence time and spectral bandwidth. When RI2C exceeded 1000, the rate of decline in the RMSs slowed, providing a reference value for the degree of temporal coherence necessary to achieve uniform irradiation over a specified integration time. The final RMS value of the STPCL-Mm with the CPP was influenced by the inevitable low-frequency modulation of the CPP[27]. Lower spatial coherence resulted in a lower RMS associated with the low-frequency modulation of the CPP. In summary, we present the relationship between spatiotemporal coherence and the RMSs of uniform irradiation, offering reference values for both temporal and spatial coherence to achieve uniform irradiation.

2.3. Third-harmonic generation efficiency of STPCL-Mm

In traditional coherent third-harmonic generation for collinear phase matching, the relationship among the phase

https://doi.org/10.1017/hpl.2025.10099 Published online by Cambridge University Press

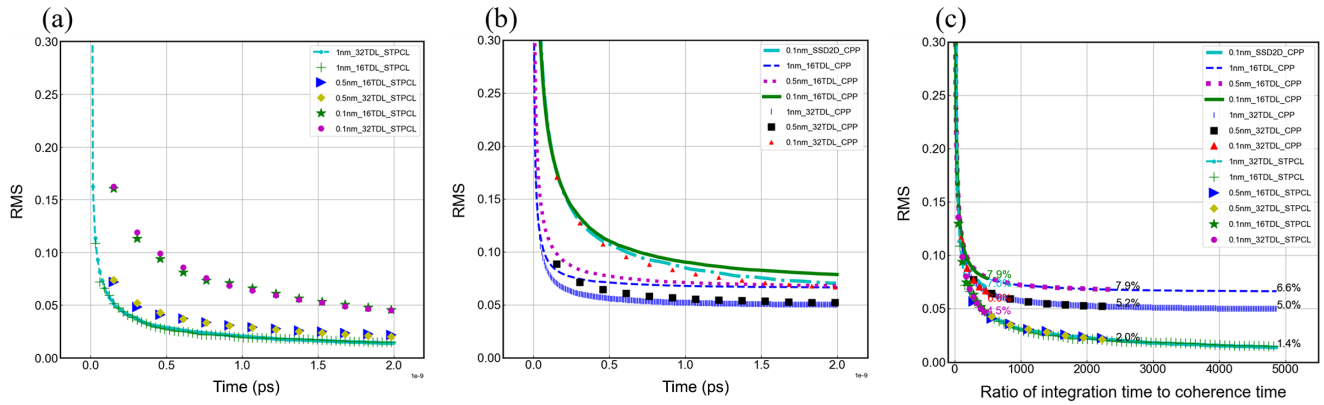


Figure 4. RMS variation of the target surface with integration time for (a) STPCL-Mm and (b) STPCL-Mm with CPP. (c) RMS variation with the ratio of integration time to coherence time.

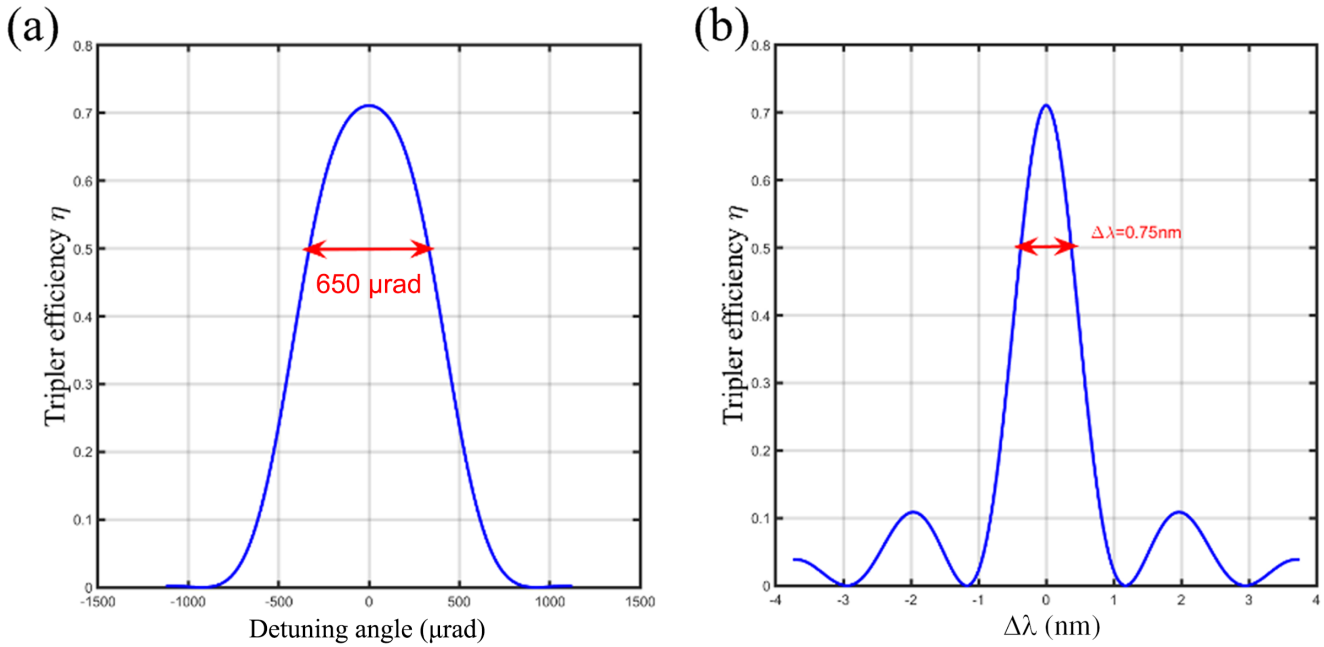


Figure 5. (a) Acceptance angle and (b) acceptance bandwidth of type-I third-harmonic generation for KDP (1.5 GW/cm^2).

mismatch, divergence angle and bandwidth can be expressed as follows:

$$\Delta k = \frac{\partial(\Delta k)}{\partial \theta}\Delta\theta + \frac{\partial(\Delta k)}{\partial \lambda}\Delta\lambda. \tag{3}$$

Figure 5 illustrates the relationships among the third-harmonic generation efficiency of potassium dihydrogen phosphate (KDP) (peak power density: 1.5 GW/cm^2), divergence angle and bandwidth. Notably, achieving a third-harmonic conversion efficiency exceeding 50% requires that the fundamental laser's bandwidth be less than 0.75 nm and the divergence angle be less than 650 μrad for the traditional collinear phase-matched third-harmonic generation scheme. When the near-field beam aperture is 310 mm, the divergence angle corresponding to 32 TDL is approximately 145 μrad, which is significantly less than 650 μrad. The fundamental-frequency bandwidth of 0.75 nm corresponds to a triple-frequency bandwidth of approximately 0.25 nm. According to Figure 5(b), approximately 7% of the RMS can be achieved within 0.5 ns through the combination of STPCL-Mm and CPP irradiation, while approximately 2.5% of the RMS can be obtained through direct irradiation of STPCL-Mm. Therefore, STPCL-Mm demonstrates a superior advantage in achieving beam uniformity and smoothing within a relatively narrow bandwidth ($\leqslant$1 nm). Moreover, if the bandwidth of STPCL-Mm is further increased (1–5 nm), the conversion efficiency will inevitably decrease. A balance must be evaluated between bandwidth and efficiency. Furthermore, considering the overall demand for large-scale drives in the future, the requirements for ultrahigh bandwidths ($\geq$5 nm) and shorter wavelengths have been prioritized. The efficient generation of high-order harmonics with large bandwidths is a significant challenge that may necessitate major design changes.

https://doi.org/10.1017/hpl.2025.10099 Published online by Cambridge University Press

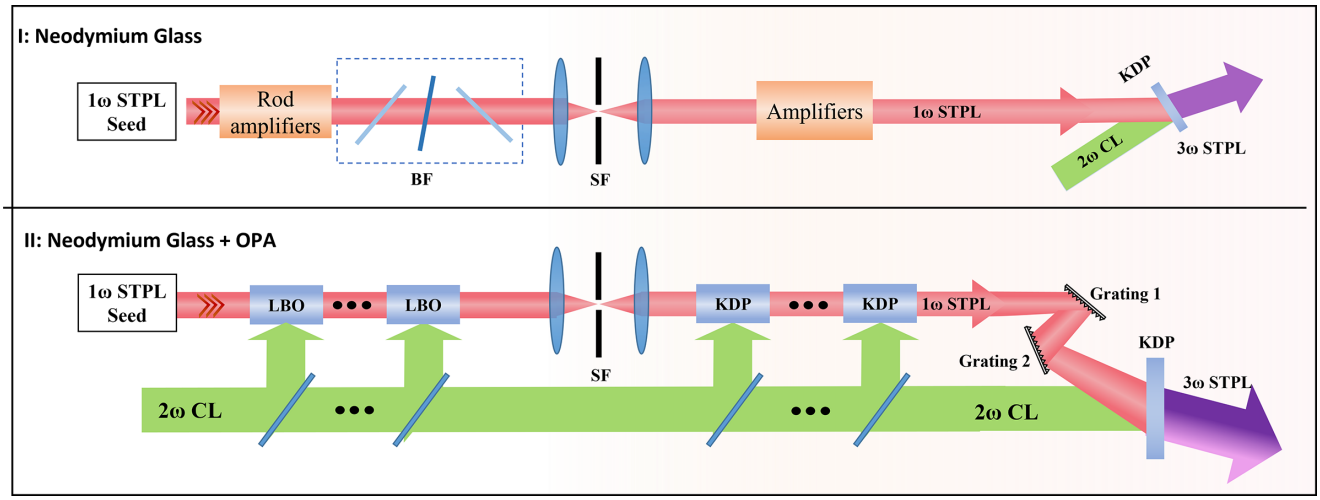


Figure 6. Scheme for the next-generation ICF laser driver based on STPCL-Mm. CL, coherence laser; STPCL-Mm, spatiotemporal partially coherent light; BF, birefringent filter; SF, space filter.

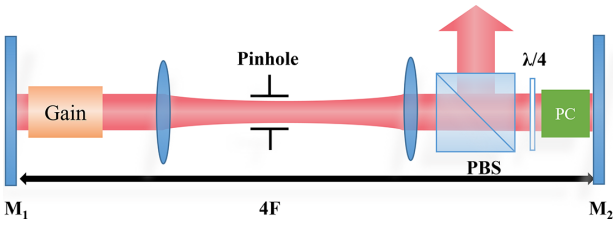


Figure 7. Schematic of the 4F imaging laser resonator.

3. Schemes for the next-generation inertial confinement fusion laser driver based on spatiotemporal partially coherent light

The laser driver based on STPCL-Mm is structurally similar to traditional lasers and consists of four main functional modules: the seed source, amplifier, beam smoothing and third-harmonic generation, as shown in Figure 6. Regarding the energy output requirements for the MJ level, when exploring new laser-driving schemes, we believe that the amplification structure will remain largely unchanged. The spatial filter is a key component of the beamline design strategy. As analyzed in Section 2, because spatially partially coherent light has a divergence angle $\Delta\theta$, certain modifications will be made to the spatial filter.

3.1. Seed source for STPCL-Mm

As the seed source for generating the STPCL-Mm, the 4F imaging laser resonator is illustrated in Figure 7. The 4F imaging resonator shares a common configuration with the spatial filters used in ICF laser drivers. Owing to its significantly larger Fresnel number compared with conventional resonators[26,29,30,32], it demonstrates enhanced resistance to diffraction effects. This characteristic enables it to accommodate a large number of high-order transverse modes. Consequently, the number of high-order transverse modes in the 4F imaging resonator exceeds that achievable in multi-mode transverse fiber laser cavities. From an imaging perspective, laser oscillation can occur between points A and A′. All imaging systems operate as low-pass filters, and their cutoff frequency is determined by the aperture stop of the system. Therefore, adjusting the aperture in the spectral plane enables precise control over the spatial coherence. In 4F imaging resonators, the frequency interval of longitudinal modes is governed by the cavity length (i.e., the optical path length between points A and A′). However, practical imaging systems are subject to aberrations that induce slight variations in the optical paths of the object points at different heights, resulting in minor deviations in the longitudinal mode interval. The number of longitudinal modes is ultimately determined by both the longitudinal mode interval and the emission spectrum of the gain medium.

3.2. Amplification routes for STPCL-Mm

To achieve laser amplification within different wavelength bandwidth ranges, we have proposed two amplification technical routes, as illustrated in Figure 6. The first amplification technology route employs neodymium-doped glass (Nd:glass) amplification, which supports a bandwidth amplification of 13 nm. However, the amplification efficiency of different wavelengths of light in Nd:glass varies, resulting in a narrowed gain range. To obtain a specific spectral shape, a birefringent filter composed of a quartz crystal and two polarizers is generally used to adjust the spectral gain during the amplification process[16], which leads to a certain shaping loss. For STPCL-Mm amplification with larger bandwidth (exceeding 13 nm), the second approach is to combine Nd:glass amplification with optical parametric amplification (OPA). This hybrid method effectively overcomes the narrow gain limitation

https://doi.org/10.1017/hpl.2025.10099 Published online by Cambridge University Press

of the Nd:glass amplifier and enhances the amplification efficiency of STPCL-Mm[42,43].

The reduced spatial coherence of the partially spatially coherent light results in an enlarged far-field focal spot. Consequently, the aperture size of the spatial filters should be adaptively adjusted based on the level of spatial coherence, necessitating modifications to the spatial filter design. Unlike traditional coherent laser systems, the initial stage spatial filter no longer requires vacuum pumping, and in some configurations, the filter itself can even be omitted.

The reduced spatial coherence (e.g., 32 TDL) significantly diminishes the impact of phase distortions and thermal distortions on the optical components, rendering these effects negligible. Consequently, relaxed manufacturing tolerances for optical components lower the system construction costs while enhancing the repetition rate of the laser driver.

During transmission and amplification, lasers passing through damaged regions or contaminants (e.g., dust) can induce modulation. In particular, under high-intensity conditions, these modulations can lead to nonlinear growth and small-scale self-focusing (SSSF), which are currently the primary factors limiting the load capacity of high-power laser drivers. Our research group has studied the influence of spatial coherence on the suppression of SSSF in the Nd:glass gain medium, and derived the empirical formula for the SSSF modulation unstable gain coefficient in partially coherent spatial light beams. In addition, we established the numerical relationship between the B-integral suppression and spatial coherence, providing a theoretical basis for enhancing the load capacity of partially coherent laser drivers[27].

3.3. *Efficiency of third-harmonic generation of STPCL-Mm*

Two third-harmonic conversion schemes are presented for STPCL-Mm with varying spectral bandwidths, as shown in Figure 6. One is the crystal cascading scheme, and the other is the method of generating third-harmonic light by utilizing angular dispersion, which is proposed by the Laser Energy Laboratory (LLE). Studies have indicated that the third-harmonic conversion efficiency in Scheme II is comparable to the performance of conventional narrowband third-harmonic generation methods[21,22].

For the narrow bandwidth STPCL-Mm (with a bandwidth of less than 1 nm) scheme, non-collinear phase matching between the small narrowband 1ω light beam and the coherent laser 2ω light beam is achieved, enabling a third-harmonic generation conversion with an output bandwidth of less than 1 nm. In contrast, for the broadband bandwidth STPCL-Mm (1–5 nm), the angular scattering broadband STPCL-Mm 1ω beam and the coherent laser 2ω beam are combined through non-collinear sum-frequency generation to produce a broadband 3ω beam. Research has shown that the third-harmonic conversion efficiency of Scheme II is comparable to that of the traditional narrowband third-harmonic generation method[21,22]. Moreover, if the wavelength of the broadband fundamental-frequency light is changed to 800 nm and a narrow band of 1053 nm is used as the pump light, a very wide bandwidth output ($\geqslant$5 nm) can be achieved near the 400 nm wavelength. This is one of the solutions developed by our laboratory to achieve a large-bandwidth output.

3.4. *Engineering complexity and feasibility of engineering implementation*

STPCL-Mm drivers exhibit parity in beamlet quantity with coherent laser architectures. Mature amplifier technologies, including Nd:glass systems and hybrid Nd:glass/OPA amplifier configurations, have introduced comparable engineering complexities across these platforms. Furthermore, critical beamline subsystems developed for coherent laser systems, such as synchronization mechanisms, temporal waveform modulation and auto-collimation, demonstrate direct adaptability to STPCL-Mm implementations, effectively accelerating the technological maturation trajectory.

4. Conclusion

For the demands for advanced uniform irradiation in direct-drive and higher-power indirect-drive systems to be satisfied, the high uniformity of laser irradiation and efficient generation of third harmonics should be balanced. In this paper, multi-transverse-mode and multi-longitudinal-mode STPCL-Mm is introduced as the laser seed source of a laser system. A possible scheme to obtain better uniform beam irradiation performance was proposed, and a systematic study of the potential architecture of the laser drive system was conducted.

This study first established a 3D light-field model for STPCL-Mm with multiple transverse and longitudinal modes and revealed how the number of transverse and longitudinal modes affects 3D light-field distributions. Subsequently, the basic characteristics of the uniform irradiation of STPCL-Mm under different conditions were analyzed and compared with those of the traditional beam smoothing scheme. The allowable bandwidth range was determined while ensuring triple-frequency efficiency and beam smoothing performance. Finally, an STPCL-Mm laser-driving architecture was proposed, providing a reference scheme for the generation, amplification and frequency conversion of STPCL-Mm. Note that a large bandwidth at short wavelengths has always been a pursuit in the field of target physics; however, it still faces significant technical challenges. Relevant research must be continuously deepened and focused on.

https://doi.org/10.1017/hpl.2025.10099 Published online by Cambridge University Press

Appendix

The intensity weight of the 2D *mn*th order of the transverse mode can be expressed as $c_{mn} = \sqrt{c_m c_n}$, where c_m is the intensity weight of the one-dimensional *m*th order of the transverse mode and c_n is the same as c_m when $m = n$. Table 1 presents the set for the c_m with the maximum transverse order of 33. The radius of TEM_{00} is 29.7 mm. Table 2 presents the set for the c_m with the maximum transverse order of 18. The radius of TEM_{00} is 42.5 mm.

Table 1. The set for c_m with the maximum transverse order of 33.

m	0	1	3	4	5	6	7
c_m (%)	2.2	2.2	2.3	2.3	2.4	2.5	2.6
m	8	9	10	11	12	13	14
c_m (%)	2.6	2.7	2.8	3.0	3.1	3.3	3.5
m	15	16	17	18	19	20	21
c_m (%)	3.7	4.0	4.4	4.8	5.2	5.5	5.7
m	22	23	24	25	26	27	28
c_m (%)	5.7	5.4	4.8	4.1	3.2	2.3	1.6
m	29	30	31	32	33		
c_m (%)	1.0	0.6	0.3	0.2	0.1		

Table 2. The set for c_m with the maximum transverse order of 18.

m	0	1	3	4	5	6	7
c_m (%)	4.6	4.8	5.1	5.5	6.0	6.6	7.4
m	8	9	10	11	12	13	14
c_m (%)	8.4	9.3	9.8	9.5	8.3	6.3	4.2
m	15	16	17	18			
c_m (%)	2.4	1.2	0.5	0.2			

Acknowledgements

This work was supported by the Strategic Priority Research Program of the Chinese Academy of Sciences (Grant Nos. 11CK020101, XDA25020203, XDA25020301 and XDA25010100).

References

1. G. C. Wang, Chinese J. Lasers **14**, 641 (1987)
2. N. G. Basov and O. N. Krokhin, Soviet Phys. JETP **19**, 123 (1964).
3. H. Abu-Shawareb, R. Acree, P. Adams, J. Adams, B. Addis, R. Aden, P. Adrian, B. B. Afeyan, M. Aggleton, and L. Aghaian, Phys. Rev. Lett. **132**, 065102 (2024).
4. H. Abu-Shawareb, R. Acree, P. Adams, J. Adams, B. Addis, R. Aden, P. Adrian, B. B. Afeyan, M. Aggleton, and L. Aghaian, Phys. Rev. Lett. **129**, 075001 (2022).
5. D. Eimerl, E. M. Campbell, W. F. Krupke, J. Zweiback, W. L. Kruer, J. Marozas, J. Zuegel, J. Myatt, J. Kelly, D. Froula, and R. L. McCrory, J. Fusion Energy **33**, 476 (2014).
6. E. Wolf and E. Collett, Opt. Commun. **25**, 293 (1978).
7. S. Skupsky, R. W. Short, T. Kessler, R. S. Craxton, S. Letzring, and J. M. Soures, J. Appl. Phys. **66**, 3456 (1989).
8. R. H. Lehmberg and S. P. Obenschain, Opt. Commun. **46**, 27 (1983).
9. J. Hunt and D. R. Speck, Opt. Eng. **28**, 284461 (1989).
10. S. Skupsky and K. Lee, J. Appl. Phys. **54**, 3662 (1983).
11. K. Tsubakimoto, M. Nakatsuka, H. Nakano, T. Kanabe, T. Jitsuno, and S. Nakai, Opt. Commun. **91**, 9 (1992).
12. S. Zhou, Z. Lin, and X. Jiang, Opt. Commun. **272**, 186 (2007).
13. S. P. Regan, J. A. Marozas, R. S. Craxton, J. H. Kelly, W. R. Donaldson, P. A. Jaanimagi, D. Jacobs-Perkins, R. L. Keck, T. J. Kessler, D. D. Meyerhofer, T. C. Sangster, W. Seka, V. A. Smalyuk, S. Skupsky, and J. D. Zuegel, J. Opt. Soc. Am. B **22**, 998 (2005).
14. L. Ji, X. Zhao, D. Liu, Y. Gao, Y. Cui, D. Rao, W. Feng, F. Li, H. Shi, J. Liu, X. Li, L. Xia, T. Wang, J. Liu, P. Du, X. Sun, W. Ma, Z. Sui, and X. Chen, Opt. Lett. **44**, 4359 (2019).
15. Y. Cui, Y. Gao, D. Rao, D. Liu, F. Li, L. Ji, H. Shi, J. Liu, X. Zhao, W. Feng, L. Xia, J. Liu, X. Li, T. Wang, W. Ma, and Z. Sui, Opt. Lett. **44**, 2859 (2019).
16. Y. Gao, Y. Cui, L. Ji, D. Rao, X. Zhao, F. Li, D. Liu, W. Feng, L. Xia, J. Liu, H. Shi, P. Du, J. Liu, X. Li, T. Wang, T. Zhang, C. Shan, Y. Hua, W. Ma, X. Sun, and X. Chen, Matter Radiat. Extremes **5**, 065201 (2020).
17. H. Nakano, K. Tsubakimoto, N. Miyanaga, M. Nakatsuka, T. Kanabe, H. Azechi, T. Jitsuno, and S. Nakai, J. Appl. Phys. **73**, 2122 (1993).
18. H. Nakano, N. Miyanaga, K. Yagi, K. Tsubakimoto, T. Kanabe, M. Nakatsuka, and S. Nakai, Appl. Phys. Lett. **63**, 580 (1993).
19. S. P. Obenschain, S. E. Bodner, D. Colombant, K. Gerber, R. H. Lehmberg, E. A. McLean, A. N. Mostovych, M. S. Pronko, C. J. Pawley, A. J. Schmitt, J. D. Sethian, V. Serlin, J. A. Stamper, C. A. Sullivan, J. P. Dahlburg, J. H. Gardner, Y. Chan, A. V. Deniz, J. Hardgrove, T. Lehecka, and M. Klapisch, Phys. Plasmas **3**, 2098 (1996).
20. B. Xu, Y. Wan, X. Fan, and Z. He, Adv. Photonics **6**, 016006 (2024).
21. J. Zhang, P. Li, R. C. C. Cheung, A. M. H. Wong, and J. Li, Adv. Photonics **5**, 036001 (2023).
22. D. Kupka, IEEE J. Quantum Electron. **48**, 790 (2012).
23. J. W. Bates, J. F. Myatt, J. G. Shaw, R. K. Follett, J. L. Weaver, R. H. Lehmberg, and S. P. Obenschain, Phys. Rev. E **97**, 061202 (2018).
24. A. E. Willner and H. Zhou, Adv. Photonics **6**, 010502 (2024).
25. E. Wolf, *Introduction to the Theory of Coherence and Polarization of Light* (Peking University Press, Beijing, 2014), p. 61.
26. R. Chriki, S. Mahler, C. Tradonsky, V. Pal, A. A. Friesem, and N. Davidson, Phys. Rev. A **98**, 023812 (2018).
27. A. E. Siegman, *Lasers University Science Books* (University Science Books, Mill Valley CA, 1986), p. 208.
28. Z. A. Chen, X. Q. Zhang, Y. L. Zhang, J. H. Tang, R. F. Wang, and J. Q. Zhu, Chinese J. Lasers **51**, 2201011 (2024)
29. H. Cao, R. Chriki, S. Bittner, A. A. Friesem, and N. Davidson, Nat. Rev. Phys. **1**, 169 (2019).
30. M. Nixon, B. Redding, A. A. Friesem, H. Cao, and N. Davidson, Opt. Lett. **38**, 3858 (2013).
31. B. Redding, M. A. Choma, and H. Cao, Nat. Photonics **6**, 355 (2012).
32. K. P. Zhang, X. Q. Zhang, F. Tao, Y. L. Zhang, H. Wei, F. L. Yang, and J. Q. Zhu, Chinese J. Lasers **49**, 2401002 (2022).
33. T. R. Wang, X. Q. Zhang, Y. L. Zhang, F. L. Yang, J. H. Tang, A. Z, and J. Q. Zhu, High Power Laser Sci. Eng. **12**, e31 (2024).
34. G. D. Ma, C. Y. Shen, J. X. Li, L. Z. Huang, C. Isil, F. O. Ardic, X. Yang, Y. Li, Y. Wang, M. S. S. Rahman, and A. Ozcan, Adv. Photonics Nexus **6**, 066008 (2024).
35. R. Sun, T. Fu, Y. Huang, W. Liu, D. Z, and H. Chen, Adv. Photonics Nexus **3**, 026007 (2024).
36. J. Q. Zhu, *Design and Development of Large High-Power Laser Devices* (Shanghai Scientific and Technical Publishers, Shanghai, 2020), p. 78.

https://doi.org/10.1017/hpl.2025.10099 Published online by Cambridge University Press

37. X. P. Zhang, X. Q. Zhang, Y. Zhang, G. Zhang, S. Xu, S. Zhou, and J. Zhu, Laser Photonics Rev. **20**, e01544 (2026).
38. S. Y. Xu, X. Q. Zhang, Y. L. Zhang, G. W. Zhang, X. P Zhang, S. L. Zhou, and J. Q. Zhu, https://cstr.cn/31253.11.sciencedb.25076 (2025).
39. S. F. Liew, S. Knitter, S. Weiler, J. F. Monjardin-Lopez, M. Ramme, B. Redding, M. A. Choma, and H. Cao, Opt. Lett. **42**, 411 (2017).
40. J. E. Rothenberg, J. Opt. Soc. Am. B **14**, 1664 (1997).
41. J. He, P. Li, X. Chai, and L Wang, Chinese J. Lasers **49**, 1105001 (2022).
42. C. Dorrer, M. Spilatro, S. Herman, T. Borger, and E. M. Hill, Opt. Express **29**, 16135 (2021).
43. N. Ekanayake, M. Spilatro, A. Bolognesi, S. Herman, E. M. Hill, and C. Dorrer, Opt. Express **31**, 17848 (2023).

https://doi.org/10.1017/hpl.2025.10099 Published online by Cambridge University Press